| DIE ERDE **142** 2011 (3) | Contributions to Geoarchaeology | pp. 289-313 |
|---|---|---|

• *Geophysical prospection – Terrain modelling – 3D visualisation – Arid environments*

**Jonas Berking, Julia Meister, Burkart Ullrich, Michael Schott, Georg Kaufmann** and **Brigitta Schütt**

# Geoarchaeological Methods for Landscape Reconstruction at the Excavation Site of Naga, Central Sudan

*Geoarchäologische Methoden zur Landschaftsrekonstruktion an der Ausgrabungsstätte von Naga, Zentralsudan*

With 11 Figures and 3 Tables

The archaeological excavation site of Naga, remains of a Meroitic city, is located in the semi-arid region along the fringe of the north-eastern Sahel and the south-eastern Sahara desert, in central Sudan, 150 km north of Khartoum and 40 km south of the Nile. During its heyday the city was a highly developed central place, with a large population and a booming economy. Naga has been the object of archaeological research for several decades – and of geoscientific investigation since 2008. The first step for the investigation was to select adequate methods that combine the advantages of various subdisciplines and approaches. The study presented employs techniques from terrain modelling, geophysics and environmental analytics to evaluate field data with the aim of a comprehensive landscape reconstruction.

## 1. Introduction

Naga was a major city in central Sudan from the 3rd century BCE (Before Common Era) to the 4th century CE (Common Era) (*Wildung* and *Kröper* 2006). The city was part of the Meroitic Culture, which developed in the Kingdom of Kush during the first millennium BCE. This kingdom had its first capital, Napata, north of the 4th cataract, but later moved it southward to Meroe, located between the 6th and 5th cataract (*Adams* 1974), i.e., the capitals of the Kingdom of Kush were founded in direct proximity to the Nile River. By contrast, the city of Naga was situated in the remote hinterland away from the Nile. This considerable distance from any perennial freshwater source led to the construction of one of the most fascinating geoarchaeological objects at Naga: the open water-storage basin known as the "Great Hafir" of Naga (*Fig. 1*).

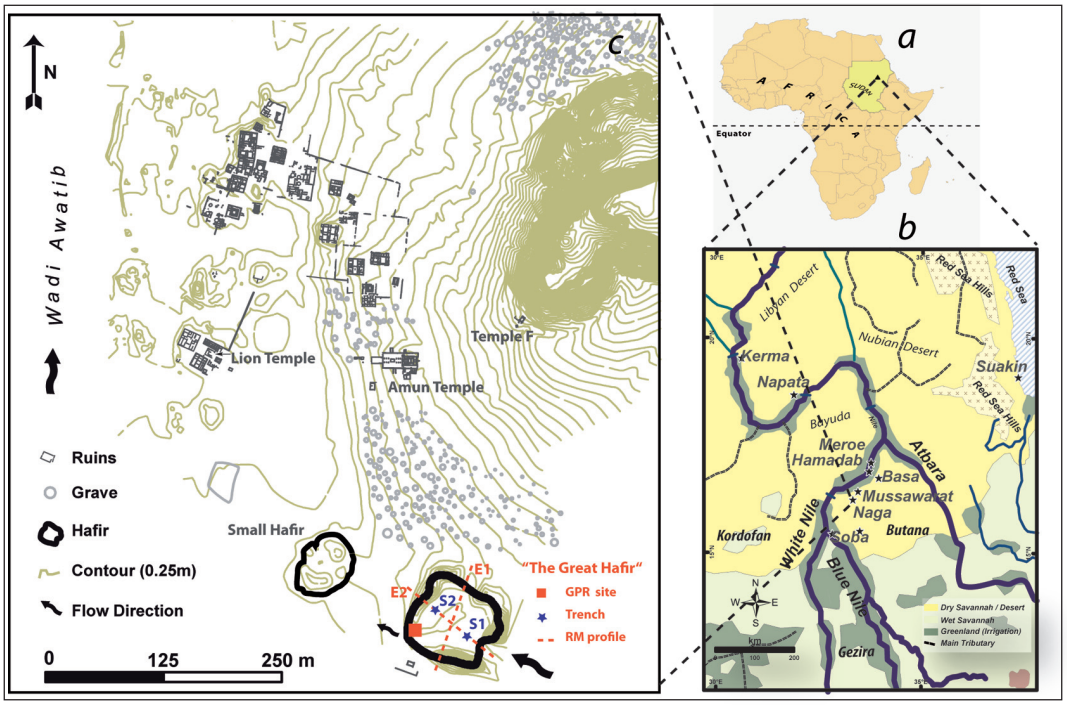


*Fig. 1* The study site and its location in NE Africa. a: Location in Africa, b: Central places during the Meroitic Period (including the capitals of the former kingdoms, Napata and Kerma), c: The city of Naga, including pertinent features / *Das Untersuchungsgebiet in NE-Afrika. a: Lage in Afrika, b: Zentralorte während der Meroitischen Periode (einschl. der Hauptstädte der früheren Königreiche, Napata und Kerma), c: Die Stadt Naga (mit erhaltenen Anlagen)*

### *1.1 Scope of the study*

Geoarchaeology applies geoscientific methods to answer archaeological questions (*Rapp* and *Hill* 2006). The present study aims to apply methods from *terrain modelling, geophysics* and *environmental analytics* in order to generate a comprehensive landscape reconstruction primarily based on field data. Our main interest is to reconstruct the palaeo-topography during Meroitic times and to evaluate the different methods used for the study. The target area presented here is the "Great Hafir", where the various methods applied to investigate surface and sub-surface topography have already been interlinked. Here information on the palaeo-topography and the combination with sub-surface sedimentological and geophysical approaches are already processed, which allows the reconstruction of the environmental situation in Meroitic times and the changes which have occurred since.

### *1.2 Study site*

The remains of the city of Naga are located on the right bank of Wadi Awatib, about 150 km north of the Sudanese capital Khartoum, and about 40 km south of the River Nile (*Fig.1*). Wadi Awatib is an ephemeral stream that drains an area of 2360 km² and enters the Nile between the 5th and the 6th cataract, close to the town of Shendi. The area is characterised by one rainy

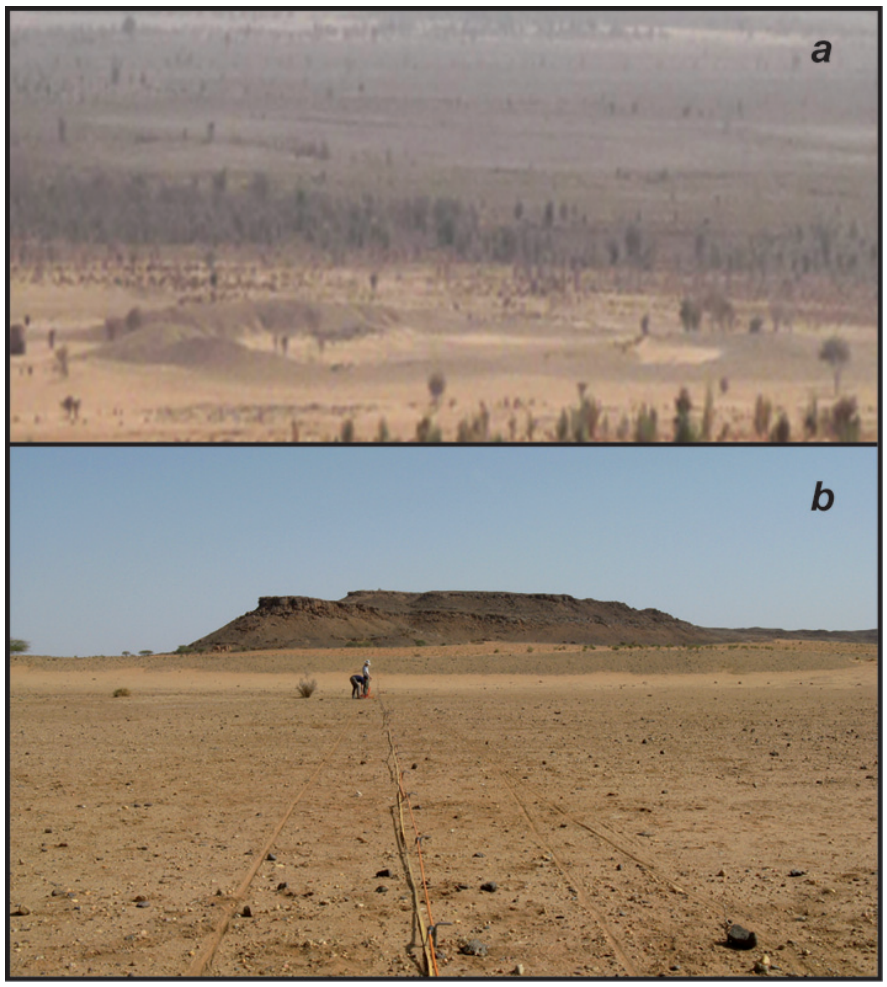


*Fig. 2* Photos of the Great Hafir. a: The Great Hafir of Naga from an eastern perspective, background: Wadi Awatib; b: Resistivity measurements in the "Great Hafir Basin", background: Gebel Naga (photos: authors)
*Fotos vom Großen Hafir. a: Das Große Hafir von Naga aus östlicher Perspektive, im Hintergrund das Wadi Awatib. b: Widerstandsmessung im Großen Hafir, im Hintergrund der Gebel Naga*

season per year occurring during summer. Average annual rainfall totals 95 mm (*Berking* and *Schütt* 2011); its temporal variability and spatial distribution are virtually unknown. Most of the rainfall results from the northward shift of the Intertropical Convergence Zone (ITCZ), which produces short and heavy convective rain events (*Berking* et al. 2010). The groundwater table in the wadi is about 75 metres below the surface, measured in two wells close to the excavation site of Naga (*Berking* et al. 2010). The groundwater is of fossil origin and is not regenerated by present-day rainfall (*M. Edmunds,* pers. comm.).

Both sides of Wadi Awatib are flanked by escarpments formed in Cretaceous sandstones, rising

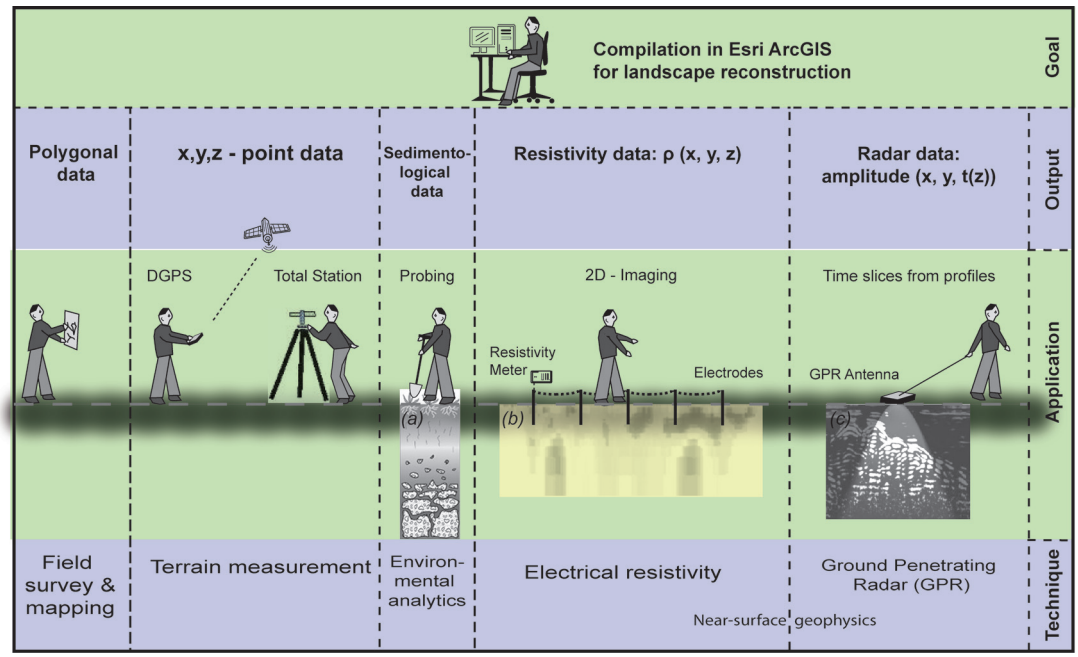


*Fig. 3* Applied methods for landscape reconstruction; with sketches of (a) hand-dug trench; (b) resistivity section; and (c) radargram / *Die zur Landschaftsrekonstruktion angewendeten Methoden; mit Skizzen zu (a) angelegtem Schnitt, (b) Widerstandsmessungen und (c) einer Georadarmessung*

up to 90 m above the valley bottom. These mesas shape the open landscape, and Meroitic temples and other sites such as Naga are often located directly at the footslopes of these ridges (*Berking* and *Schütt* 2011). Soils along the footslopes are red-brown Regosols, whereas in the upper part of the hillslopes and on top of the mesas soils show only initial development. Fluvisols predominate in the alluvial plain. In these Fluvisols, ascending soil water and evaporation cause the formation of sub-surface incrustations (*Berking* and *Schütt* 2011).

The entire area is characterised by sparse, drought-resistant vegetation, adapted to the local climatic conditions and modified by land use. *Acacia tortilis* and *Acacia mellifera* are the most prominent tree species, occurring either as riverine forest or in little patches next to the riverbeds, here associated with *Astrebla s*. and *Panicumturgidum* (*Aktar-Schuster* and *Mensching* 1993). Whereas the vegetation in the middle and lower course of Wadi Awatib shows the typical contracted pattern of drylands, a dense vegetation cover occurs in its headwater areas.

The founding of the city of Naga cannot be dated precisely. Its development possibly started in the 3rd century BCE (*Wildung*, pers. comm. 2009). Naga is regarded as one of the major towns during the late Meroitic phase. Meroitic society is characterised by both Egyptian and African attributes, and Naga also displays remarkable Hellenistic style elements (*Wildung* and *Kröper* 2006, *Wolf* et al. 2008). The site of the city includes various constructions such as temples, administrative buildings and cemeteries. The city covers an area of about 1.2 km$^2$ (121 ha) (*Fig. 1c*).

Today the area is only sparsely settled by peasants or semi-nomads, who raise cattle and live on runoff-fed agriculture, cultivating sorghum in the floodplains of Wadi Awatib (*Gabriel* 1997).

At least since Meroitic times, floodwater harvesting has been practised in the area, by collecting surface water in artificial basins, known as hafirs (Arabic: dig). Hafirs are dug into the ground. The resulting depressions are encircled by walls built of the excavated material. The use of small hafirs is still common in the area, and their water is predominantly used for irrigation and for cattle farming. The Great Hafir of Naga (*Fig. 2*) is located on the right river bank of Wadi Awatib, about 0.5 km upstream of Naga at the confluence of a minor tributary. Its construction dates back to Meroitic times; at present it is inactive owing to siltation (*Kleinschrot* 1984, 1986, *Hinkel* 1991). A similar hafir at Musawwarates Sufra, about 30 km NE of Naga, also dating from the Meroitic phase, was studied using geophysical and archaeological methods (*Scheibner* 2004).

## 2. Methods and Data Processing

To reconstruct the past topography, the data derived from the different approaches were classified and geo-coded applying ESRI ArcGIS 9.3 (*Fig. 3*). Based on these data, a model for the present topography is generated, from which the past topography is constructed by integrating geophysical and sedimentological datasets. Visualisation of the surface models is operated applying the software Surfer 9.0 from Golden Software.

### *2.1 Relief measurements and terrain-model processing*

The relief of landscapes can be determined by various methods. These include topographic maps (*Eklundh* and *Mårtensson* 1995), remote sensing data by airborne and photogrammetric missions (*Gruen* 2008), or ground measurements (Total Station, GPS, manual survey – e.g. *Wainwright* and *Mulligan* 2004, *Zhou* et al. 2008). The relief determined by these methods is generally given as (x,y,z)-data points, which can then be processed for further analysis. Once the processed data are available, terrain models can be built (cf. *Tonini* et al. 2008, *Burrough* and *McDonnell* 1998). A comprehensive introduction to digital-image procession and terrain modelling is given in *Peckham* and *Jordan* (2007) and *De By* (2001). For both archaeological and geographical precision, the comparison and best fit of such data is of great interest and is presented in the following paragraphs.

#### 2.1.1 On-site and off-site relief measurements

Surface topography was measured on-site with a Differential Global Positioning System (DGPS). Differential Global Positioning Systems use independent correction signals from stationary bases to improve the data quality of the standard GPS data (Thales Navigation 2004). As terrestrial correction signals were not available, we used an ASHTECH ProMark2 as a base station, located within a range of 5 km of the survey area and two GPS devices acting as hand-held mobile rovers. According to the manufacturer's information (Thales Navigation 2004) the post-processed DGPS data should then provide sub-metre accuracy in both horizontal and vertical dimensions, making it suitable for precision mapping, although data quality is highly dependent on environmental conditions, in many cases by shadowing effects (*Bubenzer* et al. 2007). DGPS data were obtained by two means:

1. A kinematic survey was done, with a one point per second interval, covering the study site with approximately 100 000 distinct point values. On this data base, even small changes

in topography were measured. Areas of special interest, like the surroundings of buildings or the Great Hafir, were mapped in even higher resolution. Such surveys have shown the potential of producing Digital Elevation Models (DEMs) of excellent quality with precisions in the sub-metre range (*Capra* et al. 2002, *Grunwald* and *Barak* 2003, *Forte* 2000).

2. Single points of interest were recorded by stationary survey. Several minutes of data logging allowed the precision to be improved and provided interpolation points of high reliability.

Post-processing was done applying Magellan's MobileMapper software package (version 3.3), which rectifies the rover data according to the correction signals from the base station.

Tachymetric data corresponding to the tachymetric survey were included for validation of DGPS data (data were kindly provided by *A. Riedel* with permission from *U. Weferling* 2008). The tachymetric data were collected during an earlier campaign in which parts of the study site were surveyed with a total station with a vertical precision of approximately 0.25 m, resulting in a dataset of several thousand elevation points. The tachymetric data were provided in CAD files, coded in a local coordinate system with an arbitrary site datum. The data had to be calibrated using DGPS measurements to geo-code them into a global net and were transferred relative to absolute heights via GIS software.

Remote sensing data as provided from Earth observation images allow off-site measurements of surface topography or spectral reflectance data. Here, high resolution RGB/NIR imagery from the IKONOS-2 satellite (1 m spatial resolution, acquisition date 2006-02-19) and DEM derivates of the Terra satellite mounted advanced spaceborne thermal emission and reflection radiometer (ASTER) (30 m spatial resolution, acquisition date 2005-02-21), as well as SRTM-3 elevation data (90 m spatial resolution, acquisition date 2001, revised in 2009), were incorporated to support fieldwork and assist geomorphological mapping in the GIS environment.

### 2.1.2 Terrain model

Digital Elevation Models (DEM) give a 2.5D representation of the surface, where each raster cell has a value which translates into absolute height. DEMs usually come as grayscale 2D image files and thus are not able to give a true representation of the 3D space because the value of a raster cell corresponds to the height of the terrain from a bird's eye view; therefore, for example, caves cannot be displayed. As presented in *Peeters* et al. (2006) and *Vogel* and *Märker* (2009), we used a deductive, top-down approach for relief reconstruction, stressing the initial need for a high-quality model as errors accumulate with each data set added.

To transform point-based elevation data into area information, different interpolation methods can be used. These include local neighbourhood methods such as Inverse Distance Weighting (IDW), Triangulated Irregular Networks (TIN), geostatistical methods (kriging) and polynomial functions (splines). The available algorithms are suitable for either (i) different kinds of data-point distribution or (ii) different kinds of desired result (*Hengl* and *Evans* 2009). The interpolation techniques were compared and evaluated (*Mitas* and *Mitášová* 1999, *Algarni* and *El Hassan* 2001, *Hengl* and *Evans* 2009) partly favouring IDW and often favouring spline interpolations (*Mitášová* and *Hofierka* 1993). On the basis of this operating experience, we applied spline interpolations for generating the terrain model of the study site. The DEM was processed as a GeoTiff raster file to enable the

application of other methods on a cell to cell basis. The resulting terrain model, here with a cell size of 1 m, was then used for all geometric purposes and constituted the basis for volumetric calculations or visualisations.

### *2.2 Geophysical prospection*

Geophysical prospecting techniques are applied if spatial data are needed for a detailed description of subsurface structures. The choice of method, or combination of methods, depends on the depth and dimension of the structures to be surveyed, the required resolution and the measurement conditions of the specific site. Successful application requires a contrast in the physical properties between the sub-surface structures and their surroundings. Good overviews of the different methods in applied geophysics are given by *Telford* et al. (1990) or *Knödel* et al. (1999).

The dimension of geoarchaeological features sized 1 m to 10 m can be targeted by environmental and engineering geophysical methods, which cover the range between large-scale exploration geophysics and archaeological geophysics in the submetre dimension. Geophysical prospection techniques were successfully applied mainly to reveal and delineate archaeological remains. Integrated approaches combining different geophysical methods proved to be effective tools as presented in *Drahor* 2006, *Cardarelli* and *di Filippo* 2009. Geophysical techniques were applied even for the survey of pedo- and sedimentological targets (*Leopold* et al. 2010, *Siart* et al. 2010).

*Shaaban* and *Shaaban* (2001) as well as *Weinstein-Evron* et al. (2003) demonstrated that the combination of resistivity methods and ground-penetrating radar is suitable for the detection of archaeological remains in arid environments. The related petrophysical parameters, electric resistivity ρ and electric permittivity ε vary within a range depending on type of rock and minerals, the pore space geometry and saturation and salinity of the pore fillings (*Schön* 1983).

#### 2.2.1 2D direct-current (DC) resistivity

The electrical resistivity of sedimentary structures depends on the physical properties of the material, mainly the mineral composition, the pore volume and the water saturation (*Kneisel* 2006). Electrical resistivity values can vary over several orders of magnitude, which is challenging to interpret and often quite ambiguous. Therefore, verification of the results is needed, e.g. from direct probing (e.g. *Hecht* 2007).

Resistivity measurements use a direct current, which is injected into the ground via two current electrodes inducing a potential field, which is then measured at two potential electrodes (*Ullrich* et al. 2007). Depending on the setup of the electrodes, different geometry factors are used to derive the measured apparent resistivity of the subsurface. The most probable resistivity distribution is then calculated from the measured apparent resistivity values using an inversion routine. The inversion scheme adjusts an initial starting model of the sub-surface resistivity distribution through several iterations, trying to reduce the differences between calculated and measured apparent resistivity values. The accuracy of the result obtained from the inversion is monitored through the root-mean-square error (RMS) of the differences between measurements and model.

To obtain information about the interior structure of the sediments in the Great Hafir, DC resistivity measurements were carried out along two profiles, E1 and E2 in the Hafir basin, using the multi-electrode resistivity meter GeoTom (GeoLog, Germany, *Figs. 1* and *2*). A Wenner configuration was chosen because it provides good resolution for layered structures (*Kneisel* 2006) and is relatively insensitive to minor topography changes. The

*Tab.1* Coordinates of investigated profiles in the Great Hafir Basin (location see *Fig.1*)
*Koordinaten der untersuchten Profile im Becken des Großen Hafirs (vgl. Fig.1)*

| Type | Profile (*Fig. 1*) | Location (*Fig. 1*) | UTM E (36 N) | UTM N (36 N) | Length / depth / area |
|---|---|---|---|---|---|
| **Resistivity** | E1 | Start<br>End | 529607<br>529672 | 1798058<br>1798242 | 2 profiles each 198 m (with 100 electrodes and 2 m spacing), Calculated model depth: 15 m |
| | E2 | Start<br>End | 529703<br>529560 | 1798059<br>1798196 | |
| **Sediments** | S1 | Along E2 | 529659 | 1798098 | Profile depth 1.70 m |
| | S2 | Along E2 | 529604 | 1798155 | Profile depth 1.30 m |
| **GPR** | R | A (x=0,y=0) | 529529 | 1798108 | 31 profiles each 20 m, total area 300 $m^2$, depth of penetration: 1.5 m |
| | R | B (x=20,y=0) | 529548 | 1798114 | |
| | R | C (x=20,y=15) | 529552 | 1798101 | |
| | R | D (x=0, y=15) | 529533 | 1798094 | |

apparent-resistivity data were collected with roll-along sections of 50 electrodes, spaced at 2 m distance, resulting in a total profile length of 198 m. Additionally, two test pits (S1, S2) on profile E1 were investigated to verify the expected near-surface sedimentary structures (*Fig. 1*). The measured sets of apparent resistivity data were processed with the software package DC2DInvRes (*Günther* et al. 2006, *Rücker* et al. 2006). For the 2D modelling we used 96 % and 99 % of the measured 992 apparent-resistivity data points from profiles E1 and E2 respectively. 2D modelling including the topography of the shallow Hafir walls did not show any remarkable effect on the resistivity distribution.

### 2.2.2 Ground-penetrating radar (GPR)

Ground-penetrating radar is a noninvasive geophysical technique that is able to provide high-resolution information about shallow sub-surface structures (*Neal* 2004). With this method, high-frequency electromagnetic waves are emitted, which travel through the sub-surface. A transmitting antenna is moved over the ground and radiates distinct pulses of electromagnetic waves (typically in the MHz to GHz range) into the sub-surface. The travel time through the sub-surface depends, among other factors, on the dielectric permittivity, which itself depends on the mineral assemblage and the water content of the soil. At some interfaces, e.g. sedimentary layers or changes in soil or rock type, some of the wave energy is back-scattered, as the electromagnetic wave is reflected or diffracted (*Gómez-Ortiz* et al. 2007). The reflections of the electromagnetic waves are recorded in the receiver antenna and can be converted into the depth of the interfaces, using the electromagnetic wave velocity obtained from hyperbolas in the recording. For a more complete description of the basics of GPR, see *Reynolds* (1997) and *Neal* (2004), among others.

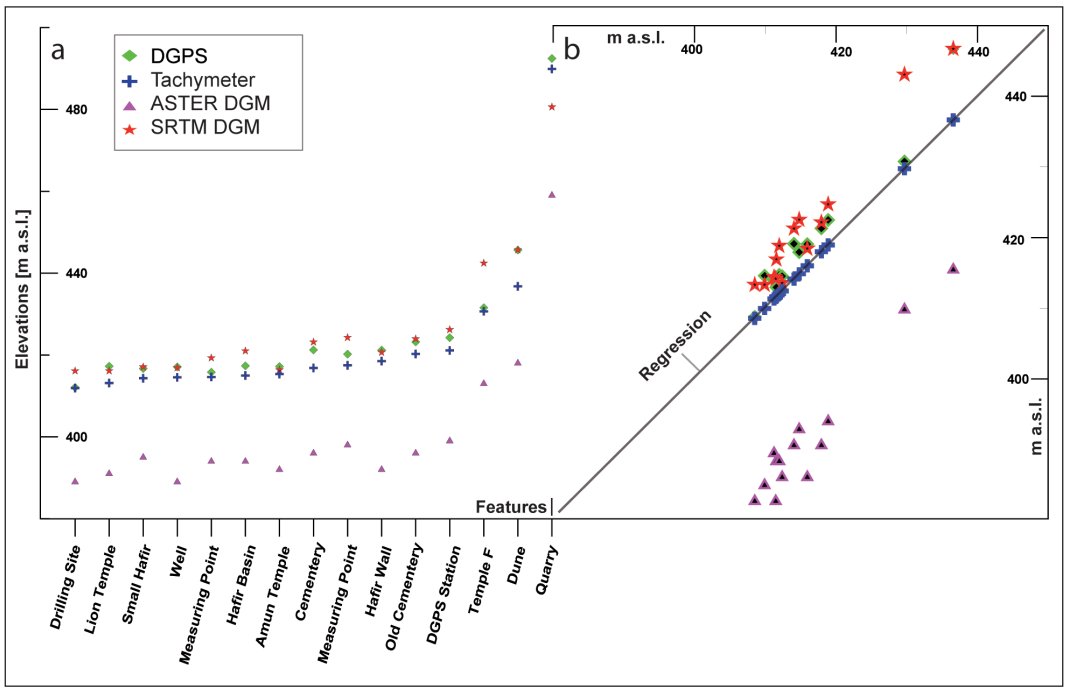


*Fig. 4* Mapped features with their absolute elevations; a: based on the different elevation datasets; b: absolute height deviation against the terrain model (regression line). Location of the features is shown in *Figure 6.* / *Aufgenommene Features mit ihrer absoluten Höhe; a: basierend auf den verschiedenen Höhendatensätzen; b: Abweichungen der absoluten Höhen gegen das Höhenmodell. Die Verortung der einzelnen Features ist in Figur 6 dargestellt.*

In the western part of the hafir, we conducted GPR surveys to detect the wall structures in the sub-surface of the hafir. The basic question was whether the opening was created during the construction phase for a specific purpose or whether it resulted from a post-Meroitic wall-burst.

Here, a SIR 3000 system with a 500-MHz antenna (GSSI, USA) was used on an area of 15 by 20 m (*Fig. 1*). The spacing between parallel profiles was 0.5 m. The distances along the surveyed lines were recorded with a survey wheel. In total, 31 profiles were recorded, of which two were split in the field because of outcropping rock formations. The sampling time window was 42 ns. Using the average wave velocity of 0.1 m/ns, this yielded a maximum survey depth of 2.1 m. Data processing was performed to increase the signal-to-noise ratio prior to interpretation, using the software package ReflexW (*Sandmeier* 1997). Data processing comprised background noise removal and a time-zero correction.

A comprehensive overview of the spatial distribution of the reflection amplitudes is given in horizontal slices of the ground. The parallel 2D radar profiles were combined into a 3D data set and sliced in equal time-intervals of 5 ns. Thus, each slice represents a layer with an approximate thickness of 25 cm down to 1.25 m below surface.

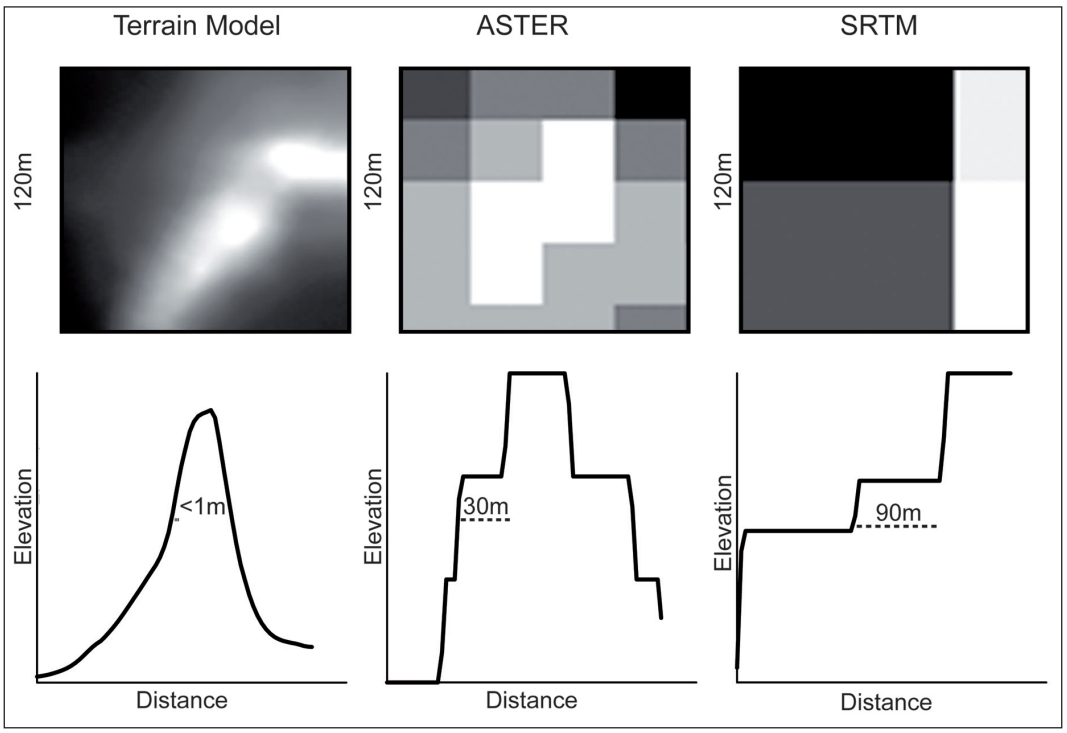


*Fig. 5* Comparison of the different digital elevation models that were investigated for applicability in our study. In a NW-SW cross-profile, a section of the north-western wall of the Great Hafir is shown, which is covered by ~4 SRTM, ~16 ASTER, > 100 on-site measured terrain model cells. The profiles (lower row) of the on-site measured terrain model and the ASTER-DEM show a wall-like structure, whereas SRTM elevation data are only able to reproduce the terrain structure fragmentarily owing to their spatial resolution of 90 m. / *Vergleich der verschiedenen Höhenmodelle und ihrer Anwendbarkeit. Hierfür ist ein NW-SW-Profil über den nordwestlichen Wall des Großen Hafirs gezeigt, welches durch ~4 SRTM, ~16 ASTER und mehr als 100 On-site-Messpunkte repräsentiert ist. Die unten gezeigten Profilkurven zeigen eine wallartige Struktur für die On-site- und ASTER-Höheninformationen, während man mit den SRTM-Daten nur eine fragmentarische Vorstellung der Landschaft erhält.*

### *2.3 Sediment sampling and laboratory analysis*

A hand-dug trench (S1) of 170 cm was excavated in the Great Hafir Basin (*Figs. 1* and *2, Tab. 1)*, and additional Pürckhauer probing (S2) was done. The lithostratigraphy was described macroscopically, and the section was systematically sampled in 10 cm steps. For S1 a chronological framework was set up by an OSL age determination (sample at 40 cm depth) and a radiocarbon age determination (sample at 80 cm depth).

OSL dating techniques were applied on aeolian quartz sands. A recent comprehensive review of OSL dating is given in *Lian* and *Roberts* (2006). Dose rates for all samples were calculated from potassium, uranium and thorium contents, as measured by gamma spectrometry in the Leib-

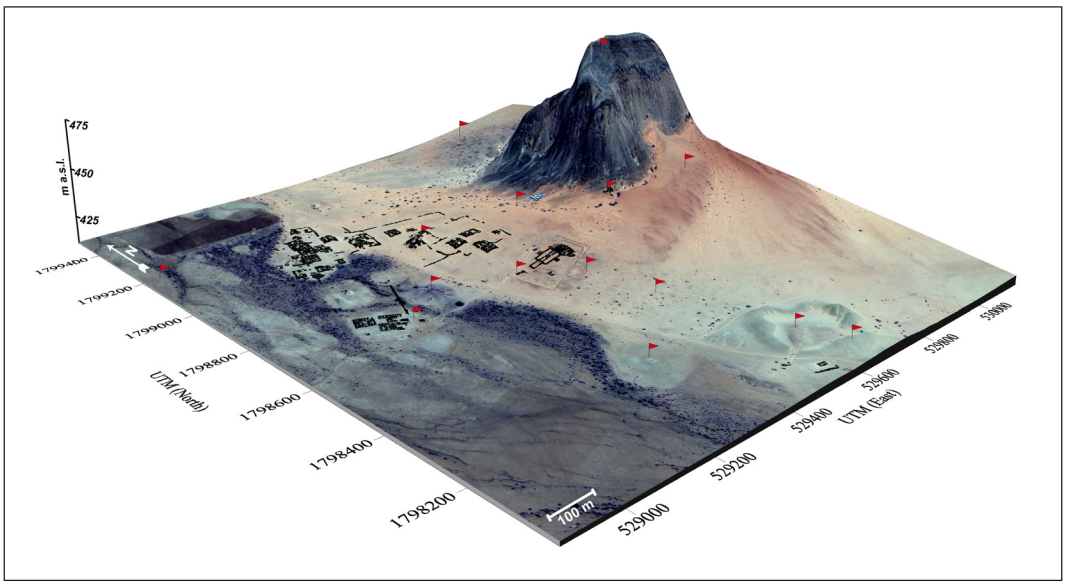


*Fig. 6* The city of Naga and its environment in a 2.5D visualisation. Red flags indicate the points (features) of *Figure 4*. The block diagram is superimposed by the true coloured IKONOS image and is 4 times vertically exaggerated. / *Die Stadt Naga in einer 2,5D-Visualisierung. Die roten Fähnchen zeigen die Messpunkte aus Figur 4. Das Blockdiagramm ist 4-fach überhöht dargestellt und durch eine echtfarbene IKONOS-Szene überlagert.*

niz Institute for Applied Geophysics (LIAG), Hannover. All OSL samples were pre-treated with standard methods for SAR protocol at the laboratories of the LIAG (*Reimann* et al. 2010). A single aliquot regenerative dose measurement protocol (*Murray* and *Wintle* 2000) was adopted for palaeodose determination at the Research Laboratory for Archaeology and the History of Art, University of Oxford (in-depth information about the applied OSL method is already published in *Berking* and *Schütt* 2011).

A boulder-sized charcoal piece was found at 80 cm depth. It was used for conventional radiocarbon dating (sample number HV 25821 at the laboratories of LIAG in Hannover, Germany). Radiocarbon ages were calibrated according to *Stuiver* et al. 1998 (in-depth information about the radiocarbon dating in *Schütt* et al. 2010).

## 3. Results

### *3.1 Terrain features*

The direct comparison of several distinct point surface measurements and their absolute elevation was evaluated and plotted (*Fig. 4a*). The four datasets available are: (i) the DGPS on-site measurements, (ii) the radiometric SRTM elevation data, and (iii) the derived ASTER elevation data, both based on off-site measurements, (iv) the tachymetric data on topography, also provided by on-site measurements. The absolute elevations resulting from the different methods show marked deviations (*Fig. 4b*).

For a distinct areal comparison of elevation datasets, we selected the NE part of the Hafir embankment to evaluate the different spatial

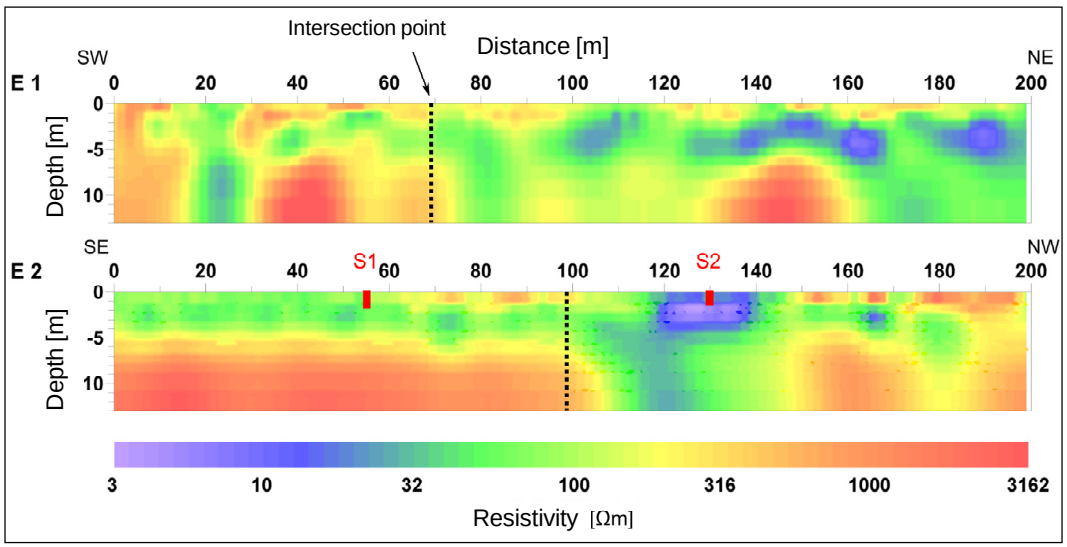


*Fig. 7* 2D resistivity sections along the profiles E1 and E2; dotted lines mark the intersection point of both profiles, location of test pit (S1) and Pürckhauer drilling (S2) marked in red. / *2D-Widerstandsverteilungen entlang der Profile E1 und E2 (punktierte Linien zeigen die Trennlinie der beiden Profile; die Lage der Testgrube (S1) und der Pürckhauer-Probe (S2) ist in rot angegeben).*

resolutions, here with the direct comparison of the space-borne SRTM and ASTER data as well as the generated terrain model. This arched landscape feature with a horizontal and vertical resolution of several metres is well represented in the terrain model, but not distinguishable in the SRTM and oddly shaped in ASTER data (*Fig. 5*).

Of the different available datasets, the tachymetric data gave the best spatial resolution and were used to generate the terrain model. Based on on-site measurements, the terrain model has various advantages in terms of surface characteristics. One possibility for a better understanding of the landscape is its visualisation in a 2.5D block diagram *(Fig. 6*). This illustration shows clearly that the city of Naga is located in the transition zone between the floodplain and the elevated foot of Gebel Naga (*Fig. 6*; *Berking* and *Schütt* 2011).

### *3.2 Resistivity measurements*

The models of the 2D resistivity distribution to a depth of 15 m are illustrated in *Figure 7*. RMS values of 21 % for profile E1 and 12 % for profile E2 were calculated. The resistivity distribution along the two profiles shows several low- and high-resistivity anomalies of different dimensions presented in different colour shades (*Fig. 7*).

Zones of high resistivities are located in the northern and southern parts of the basin and attain resistivity values ranging from 500 to 3200 Ωm (yellow, red). In both sections, these zones extend from depths of 5 m down to a maximum depth of 15 m. The high resistivity values, which increase with greater depth, indicate more compact and lower-saturated sediments and can therefore be interpreted as bedrock (sandstone) (*Fig. 8*).

Zones of remarkably low resistivity values (< 50 Ωm) are visible in both profiles, differing

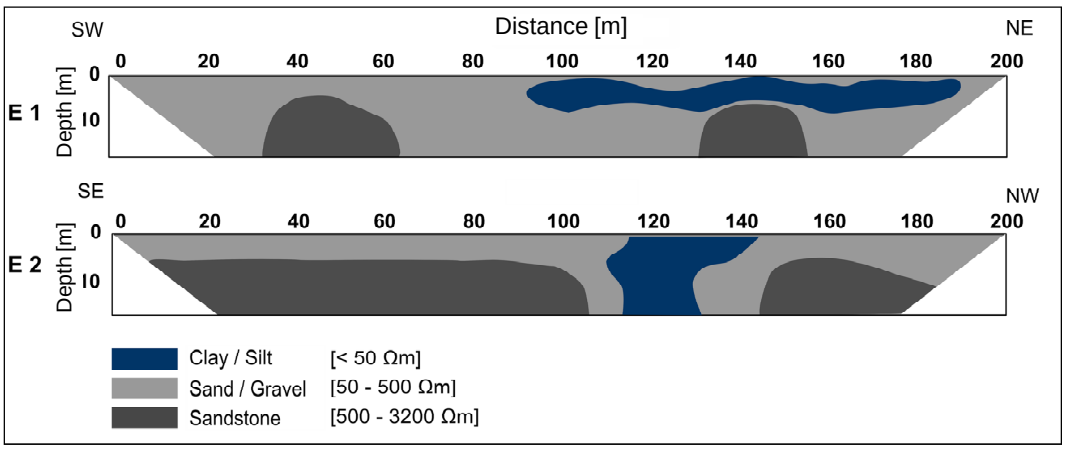


*Fig. 8* Classified sketch of the interpreted resistivity models
*Klassifikation der interpretierten Widerstandsverteilungen*

in shape and extension (blue, greenish-blue). In profile E1, the low-resistivity zone stretches from 100 to 180 m and is rather shallow with depths of down to 5 m. In profile E2, the low-resistivity zone is located between 110 and 140 m, extending to the maximum (modelled) depth of 15 m. According to sediment profile S2, these resistivity values point to fine-grained sediments (silt, clay), which can be interpreted as the slack-water deposits in the hafir basin. Intermediate resistivity values between 50 and 500 Ωm might be induced by coarser-grained sediments, which are indicated by the results from pit S1, where sand with varying gravel contents occurs (see Section 3.4 *Sediment analysis*).

High resistivity values close to the sub-surface are caused by coarser sediments (gravel, sand) in the unsaturated zone.

### *3.3 Results of the GPR survey*

The processed GPR data are depicted in selected radargrams. The registration time of 42 ns is converted to a depth of 2.1 m. An inspection of the selected radar sections shows strong reflections down to 1.5 m depth, but the locations of these reflections differ. High amplitudes at greater depths result mainly from amplification and have a low signal-to-noise ratio.

Strong reflections occur mainly in two areas. The radargrams of profiles 2 to 11 in the south show visible reflectors between 15 and 20 m. At depths between 0.50 m and 1.30 m, diffraction hyperbolas are formed, which can be seen in Profile 6 (*Figs. 9.1a* and *1*). Another reflection pattern appears in the western part of the surveyed plot, as depicted in *Figs. 9.1b* and *c (2).* The radargrams show high amplitudes at 0.60 m to 1.50 m depth. The GPR anomalies have weak to well-visible hyperbolic shapes. In the radargrams of Profiles 1 and 27 to 31, traces of reflections and diffractions are missing.

The main sub-surface structures are clearly visible as complex distribution patterns in the processed horizontal time slices. Whereas in the shallow slice (0.25-0.5 m, *Fig. 9.2a*) no anomaly pattern is visible, there are two nearly circular reflection patterns in the slice below

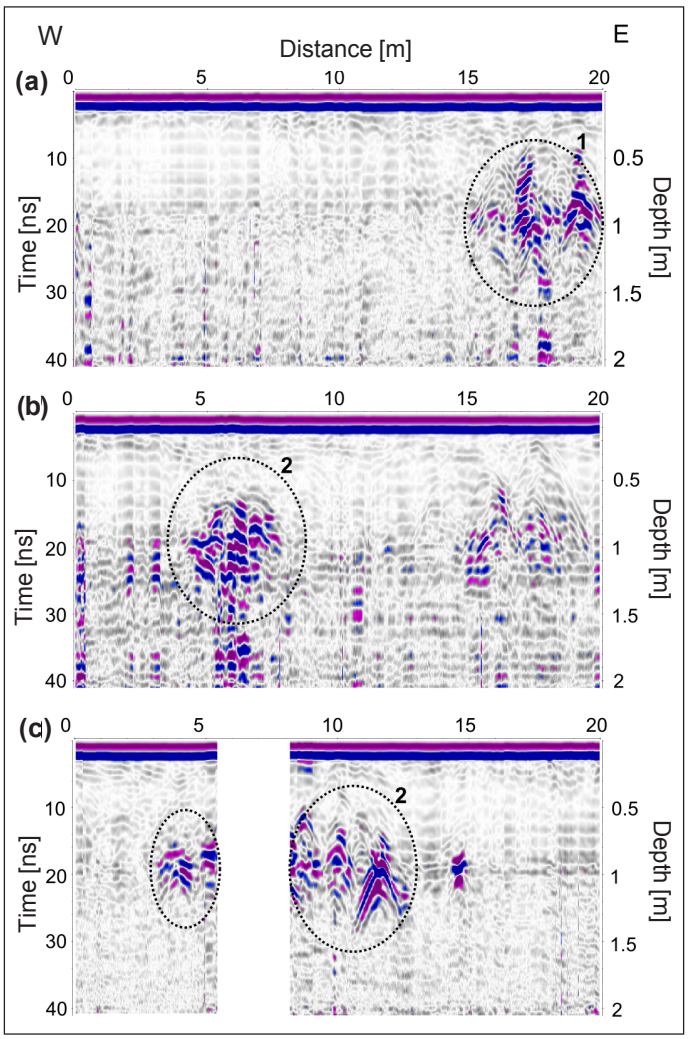


*Fig.9.1* Radar sections archieved with a 500 MHz antenna of Profiles 6 (a), 10 (b) and 17(c) at the western hafir opening (for measurement location see *Fig.1*, areas in dotted lines mark the described reflection patterns) / *Radagramme, aufgenommen mit der 500 MHz-Antenne an den Profilen 6(a),10(b) und 17 (c), an der westlichen Hafir-Öffnung (zur Lage der Messung s. Fig. 1, gepunktet umrandete Felder zeigen die beschriebenen Reflektionsmuster)*

(0.5-0.75 m, *Fig. 9.2b*). This anomaly pattern becomes sharper and wider with depth, with a size of 5 by 5 $m^2$ (1) in the southeast and 10 by 10 $m^2$ (2) right in the middle of the surveyed plot (*Fig. 9.2c*). The high-anomaly patterns indicate hard obstacles that face the radar-wave paths and magnify their signals. In the depth range from 1.0 to 1.25 m (20-25 ns), the high-anomaly pattern is partly reduced (*Fig. 9.2d*). The additional appearance of horizontal structures is possibly caused by varying amplitude levels in single profiles.

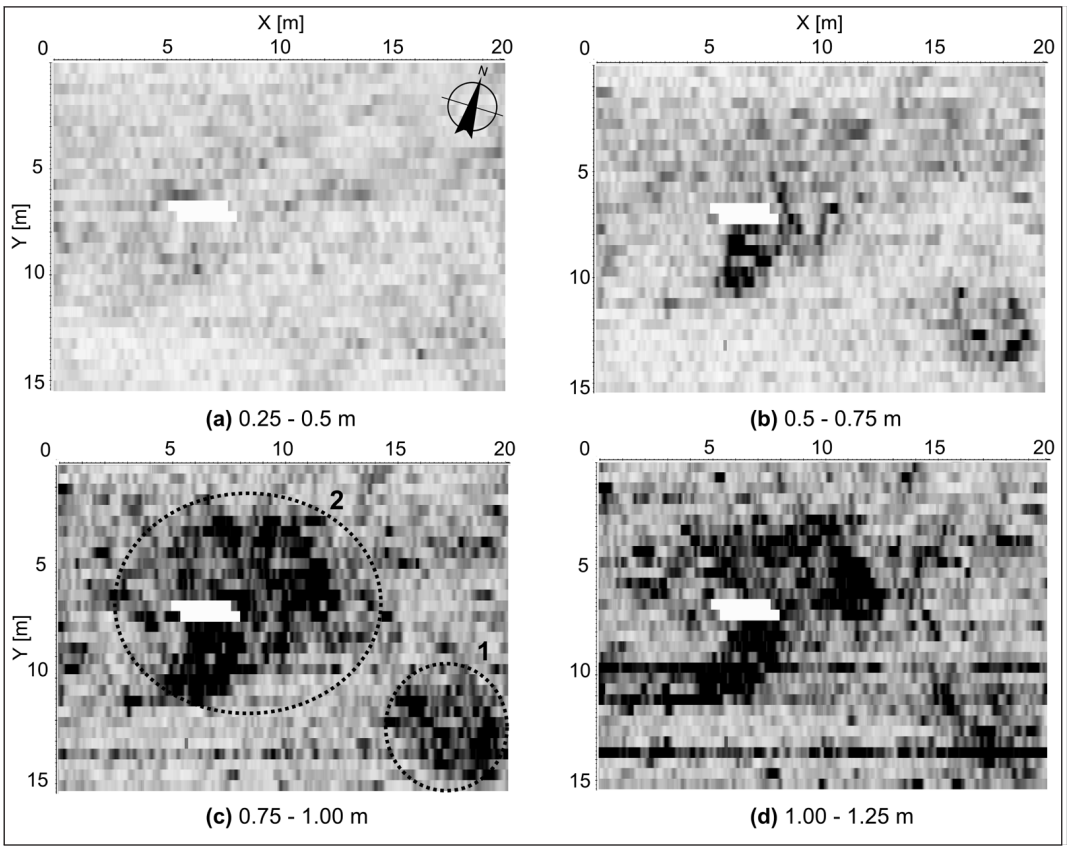


*Fig. 9.2* Selected GPR time slices at the western hafir opening, based on the processing of the radar surveying between 5 and 25 ns (dotted lines mark the reflection patterns) / *Ausgewählte Zeitscheiben der GPR-Messungen an der westlichen Hafir-Öffnung, basierend auf den Radarmessungen zwischen 5 und 25 Nanosekunden (markiert: Reflektionsmuster)*

We assume that the well-marked and extended reflection patterns in the GPR depth sections prove the existence of bedrock in the subsurface. Evidence is given by the emerging outcropping rocks in the surveyed area. The fact that all reflectors are close to these outcropping rocks leads to the conclusion that there is at least one continuous block of rock in the western part of the opening (*Fig. 9.2*). The nearly identical diffraction patterns in the radar sections southeast of the investigated area indicate the same geological setup. The high amplitudes therefore characterise the reflections at the stratigraphic boundary of the overlying sand to the underlying bedrock.

### *3.4 Sediment analysis and age determination*

At 16.263°N and 33.277°E, a hafir trench (S1) of 170 cm was systematically analysed and macroscopically interpreted (*Fig. 10, Tab. 2*). Sediments are mainly composed of medium and fine sand fractions. At 16.264°N and 33.277°E, a pürkhauer probing at 1.3 m (S2) revealed sediments with a much finer fraction (*Fig. 1,*

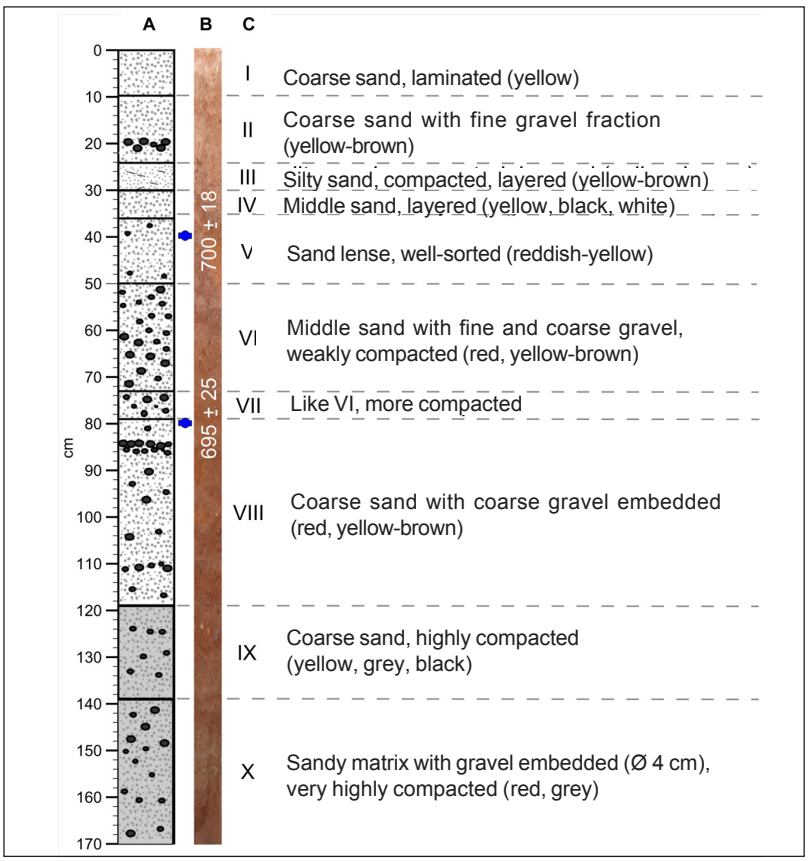


*Fig. 10* Litho- and chronostratigraphy of the hand-dug hafir trench (S1); with (A) scale and lithostratigraphy; (B) stacked photo images with age determination (blue markers), (C) layer descriptions / *Litho- und Chronostratigraphie des Hafir-Schnitts (S1); mit (A) Tiefenangaben und Lithostratigraphie; (B) zusammengesetztem Foto sowie den Altersdatierungen und (C) ihre Beschreibung*

*Tab. 1*). The sediments of S1 show marked transitions in terms of their colours from bright yellow to orange-red as well as dark brown and greyish horizons (*Fig. 10*). Layers I and II between 0 and 25 cm and VI-VIII between 50 and 120 cm depth consist of rounded to well-rounded pebbles and unsorted sandy grain sizes. The layers III–V between 25 and 50 cm depth with partly well-sorted sand and a much lower gravel fraction are mostly yellowish. The bottom layers IX and X below 120 cm are highly compacted dark greyish layers.

Two samples for age determination yielded an OSL age from a 40 cm deep quartz sand lense of 700 ± 180 years and a calibrated radiocarbon age from an 80 cm deep charcoal piece of 695 ± 25 years BP. Hence both ages are of the same age in respect of their 1-s uncertainty (*Tab. 2*).

### *3.5 Capacity and physical setting of the Great Hafir*

The Great Hafir of Naga is one of three inactive hafirs in the vicinity of the ancient city, but it is

*Tab. 2* Results of age determination (* calibrated with CalPal online, 10/05/2010)
*Ergebnisse der Altersdatierungen (* kalibriert mit Hilfe von CalPal online, 10/05/2010)*

| Method | Profile | Lab Num | Depth [cm] | Age [a BP] | STD [± a] | Calibrated time slice [AD] | $^{14}C$ Age [a] | $\delta^{13}C$ ‰ |
|---|---|---|---|---|---|---|---|---|
| OSL | S 1 | LUM 1624 | 40 | 700 | 180 | | | |
| $^{14}C$ | S 1 | HV 25821 | 80 | 695* | 25* | 1245 -1259 | 740 ± 45 | -24,5 |

the only one which can be reliably dated to Meroitic times (*Wildung* and *Kröper* 2006, *Kröper* 2006-2007; *Berking* and *Schütt* 2011). The Great Hafir is located 0.5 km upstream of the city of Naga, at the right river bank on top of a lower terrace just above the present-day alluvial plain (*Fig. 1*). The Great Hafir covers an area of 3.5 ha with a surrounding wall reaching up to 4.5 m height above the present-day surface of the inner hafir. Its catchment size totals 14.2 km$^2$ (*Tab. 3*).

The reconstruction of the Great Hafir is based on the terrain model, the geophysical prospection and the chronostratigraphy of the sediments from profile S1. The reconstruction is visualised in a 2.5D block diagram (*Fig. 6*). The deepest point of the inner hafir is located at its northern margin and reaches down to a maximum depth of 15 m (*Fig. 8*).

The well-preserved embankments, which have been only marginally eroded, have a volume of 44,000 m$^3$. To derive the volume of the hafir basin from the volume of its excavated material, it needs to be taken into account that decompaction of unconsolidated sediments during excavation causes an overestimation of the volume calculation of the piled-up material. Thus, we calculated the basin on the basis of the embankment volume, integrating a decompaction factor of 0.85 for sand-gravel mixtures (DIN 24095, *Schöwer* 2007). Finally, we derived a basin volume of 37,000 m$^3$, corresponding to a water storage capacity of up to 37 million litres (*Tab. 3*). With our estimate of the geometry of the inner basin of 100 x 40 m in size, we estimated an average basin depth of d = 9.3 m (*Fig. 11b*, see also Discussion).

## 4. Discussion

### *4.1 Terrain modelling*

We used a spline-based interpolation to generate our terrain model from our irregular relief data. Other authors consider kriging, an interpolation method based upon geostatistical parameter evaluation, which may deliver sufficient results for scattered distributed data (*Contreras* 2009), but *Burrough* (1986) states that circumstances and parameterisation must be well understood and are not easy to determine. Thus, we chose the *TopoToRaster* function (*Hutchinson* 1988, 1989), an advanced spline-based technique, which is a tool of ArcGIS 9.3. The *TopoToRaster* function produced satisfying results for DGPS data in previous studies (*Vogel* and *Märker* 2009, *Algarni* and *El Hassan* 2001). In general, DGPS data are taken as a basis to generate high-resolution DEMs, but our DGPS data did not yield a high enough quality to apply the aforementioned techniques

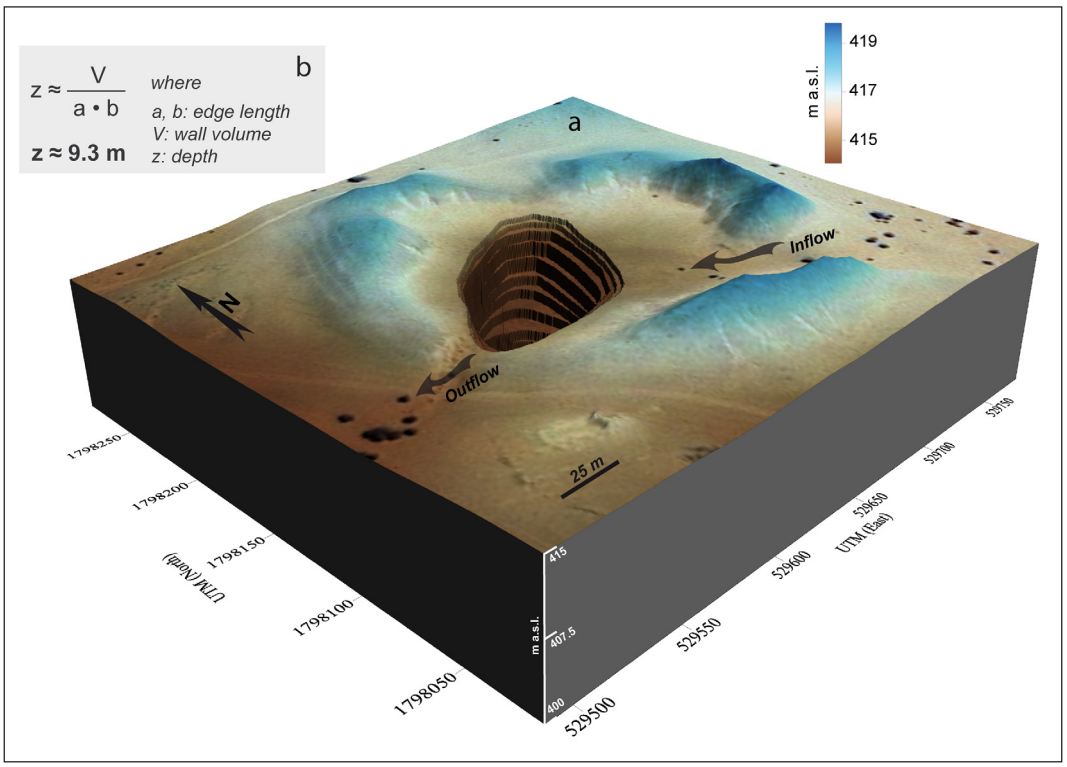


*Fig. 11* Reconstruction of the Great Hafir of Naga; (a) 2.5D block diagram (5 times vertically exaggerated) of the hafir; (b) a first-order approximation of the average depth of the inner basin / *Rekonstruktion des Großen Hafirs von Naga; (a) in einem 2,5D-Diagramm und (b) einer ersten Näherung zur mittleren Tiefe des inneren Beckens*

(Thales Navigation 2004, *Fig. 4*). High deviations and dispersion occurred during data acquisition and post-processing despite the good environmental conditions for DGPS measurements and although the device manufacturer's specifications suggest better quality (Thales Navigation 2004). Clear sources of errors could not be identified. The spatial and radiometric resolution of the off-site topographic measurements based on remote sensing data is too coarse for our study site and thus suits only as benchmarks for the given objective. However, this has to be carefully considered because correlations are challenging and data quality is often clouded by errors, as shown in our example and in previous studies (*Nikolakopoulos* et al. 2006, *Bolten* and *Bubenzer* 2006, *Bubenzer* and *Bolten* 2008, *Fig. 4*). This led us to prefer the local tachymetric ground measurements.

### *4.2 Sediment structure (resistivity measurements)*

Finally, the results of the electrical resistivity measurements were useful to differentiate between three types of subsurface structures, namely: bedrock, coarser sediments and finer deposits of the silted-up hafir basin. Nevertheless,

*Tab.3* General information about the Great Hafir / *Basisinformationen zum Großen Hafir*

| Area [$m^2$] | Diameter [m] | Wall elevation [m] | Wall volume [$m^3$] | Basin volume [$m^3$] | Catchment [$km^2$] |
|---|---|---|---|---|---|
| 350000 | 170 | Max 4.5 | $44 * 10^3$ | $37 * 10^3$ | 14.2 |
| *Fig. 1* | *Fig. 1* | *Fig. 11* | *Fig. 11* | *Fig. 11* | *Berking* et al. 2010 |

the modelled structures involve uncertainties due to technical and methodological limitations. The methodological limit caused by the equivalence principle of the resistivity models became much more important when RMS values were relatively high. These values are attributed to the fact that we used 2D imaging for the survey of 3D subsurface structures. However, we regard the data quality as adequate for a rough classification of substrate type, based on calibrations from two near-surface pits. The sediments from these two pits contain homogeneous sediments, which coincide with the two resistivity classes for the sediments. The east-west orientated bedrock formation is derived additionally from geological observations at a regional scale. In accordance with the observation that there are fault lines outside the northern part of the basin which coincide with regions of high resistivities in the resistivity sections, we assume that faults are also present in the sub-surface of the Hafir (*Bussert* 1998, *Berking* and S*chütt* 2011).

Altogether, the sediment structure indicates that the hafir was built in a natural basin with the advantage of the presence of bedrock near the surface. Because of the increase of the fine-grained sediments and their interpretation as slack-water deposits, it was possible to draw conclusions about the ancient basin's form and expansion. As these fine-grained fluvial sediments mostly accumulated in the northern part of the hafir, it seems that the area surrounded by earthen embankments had not been entirely dug out. It is far more probable that the basin itself was located only in the northern part of the inner hafir with an estimated size of 100 m * 40 m and an accessible area between walls and basin. These results correlate with the results of *Scheibner* (2004), who described the same for the Great Hafir of Musawwarat es Sufra.

Furthermore, our results support the hypothesis that the hafir reaches down approximately to the maximum model depth of 15 m or deeper, according to the distribution of low-resistivity values. The average depth of the basin depends on the underground structures and therefore varies within a certain range. It is fairly likely that the basin expansion decreased with depth, in order to cope with the excavated spoil and to facilitate water hoisting, which can be observed in many current hafirs. The excavated hafir depression was deep rather than wide, probably due to the fact that lower evaporation rates are encountered by smaller surfaces (*Hinkel* 1991, *Scheibner* 2004).

### *4.3 GPR*

Despite the low penetration depth of 1.5 m, the results of high-resolution GPR at the opening of the Western Wall have revealed underground structures that may give us important details of its original function. One of the main observations in this study is an approximately 4 m wide area between these rocks. This passage right in the centre of the wall could have been used as

an outlet. At least the shallow position of the rocks suggests that they were outcropping during Meroitic times. An additional wall opening would have allowed access to the stored water and enabled excess water to be redirected in the case of a fully filled basin. The presence of water pipes and canals near the Great Hafir in Musawwarat es Sufra (*Scheibner* 2004) or at Basa (*Kleinschroth* 1986) testifies to the existence of such Meroitic construction measures. The location of this potential outlet facing Naga and the Small Hafir supports the above-mentioned hypothesis.

### *4.4 Chronostratigraphy*

The two samples taken for age determination at 40 cm and 80 cm depth of the Hafir trench in profile S1 point to the same depositional age. We therefore interpret the hafir as an area of high sediment dynamics dominated by fluvial accumulation processes. It is assumed that the process of siltation – corresponding to the rate of accumulation – was not constant over the last 2000 years. This is also documented by the embedded depositions of well-sorted material (cf. *Folk* and *Ward* 1957). This is consistent with our idea of the Hafir as an area of high sediment dynamics. The Hafir is characterised as the end-member of a sediment cascade of its ~14 km$^2$ sized catchment. The main processes are, first, the fluvial deposition of large flash-flood events and, second, aeolian dynamics (deposition as well as deflation) during xeric/drier phases (*Berking* and S*chütt 2*011). We interpret the layers I and II between 0 and 25 cm and VI–VIII between 50 and 120 cm, with rounded to well-rounded pebbles and unsorted grain sizes, as fluvially dominated deposits, which silted up the hafir basin after its construction some 2000 years ago. The layers III-V between 25 and 50 cm depth with partly well-sorted sand and a much lower gravel fraction are interpreted as aeolian/drier/xeric phase depositions (*Nichols* 1999). The bottom layers IX and X below 120 cm are very compacted layers, which are affected by the ascending translocation of soil water and finally its evaporation and the formation of sub-surface incrustations and hence mark the transition zone to an initial saprolith horizon (*Fig. 10*, *Berking* and *Schütt* 2011).

Moreover, the calibrated radiocarbon age has to be regarded with caution since the originating wood might be allochthonous and inherit a signal from a different environment (e.g. *Bowler* 1976, *Wenske* et al. 2009, *Schütt* and *Krause* 2009).

### *4.5 Storage capacity*

Knowledge about the construction and storage capacities of Meroitic hafirs is still very limited (*Kleinschroth* 1979, 1984, 1986). The water storing capacity of a hafir depends on the depth and form of the excavated depression. The surrounding embankments did not function as dams to create supplemental water storing capacity. Most likely their function is only to pile up the excavation material (*Hinkel* 1991, *Scheibner* 2004), but they also function as a water barrier according to the water level of the annually recurring flood events.

Our calculated storage capacity of 37,000 m$^3$ is in good agreement with the study carried out by *Scheibner* (2004) at the Little Hafir at Musawwarat es Sufra. *Scheibner* estimated the hafir's volume at 33,500 m$^3$ and its depth at 8 m, which supports our hypothesis that the calculated volume of 37,000 m$^3$ corresponds to the basin's original water storage capacity.

The shape of the depression indicates a deep rather than wide basin, probably to reduce the high evaporation rates due to direct sun or wind exposure (*Estigarribia* 2008). The revealed outflow (shown in *Figure 11*) is interpreted as a spillway, which only became important when the

capacity was depleted after rare, very high rainfall events (*Berking* et al. 2010).

## 5. Conclusions

We employed various methods from geophysics, terrain modelling and environmental analytics at the site of the Great Hafir, close to the city of Naga, the capital of an ancient kingdom of the Meroitic Culture. This combination of methods led to a comprehensive landscape reconstruction model. The most important requirement is high-quality (x,y,z-) data with a spatial resolution matching the investigated targets in cell size. The addition of geophysical techniques led to remarkable results in terms of the near-surface character; however, these results should always be validated by selective sediment analysis.

The hafir, used for water storage in ancient times, is silted up with sediments and inactive at present. During Meroitic times the Great Hafir of Naga had a maximum depth of 15 m and a volume of 37,000 $m^3$.

## Acknowledgments

This study was supported by the Cluster of Excellence Exc264 Topoi – The Formation and Transformation of Space and Knowledge in Ancient Civilizations. Special thanks go to *D. Wildung* and *K. Kröper*, Ägyptisches Museum Berlin, who facilitated the fieldwork. Special thanks also to *U. Weferling* and *A. Riedel* for provision of the tachymetric data. Thanks to the two anonymous reviewers for their useful and constructive comments.

## 6. References

*Adams, W.Y.* 1974: Sacred and Secular Polities in Ancient Nubia. – World Archaeology **6** (1): 39-51

*Aktar-Schuster, M.* and *H. Mensching* 1993: Desertification in the Butana. – GeoJournal **31** (1): 41-50

*Algarni, D.* and *I. El Hassan* 2001: Comparison of Thin Plate Spline, Polynomial, $C^1$-Function and Shepard's Interpolation Techniques with GPS-Derived DEM. – International Journal of Applied Earth Observation and Geoinformation **3** (2): 155-161

*Berking, J.* and *B. Schütt* 2011: Late Quaternary Morphodynamics in the Area of the Meroitic Settlement of Naga, Central Sudan. – Zeitschrift für Geomorphologie, Supplementbände **55** (3): 1-24

*Berking, J., B. Beckers* and *B. Schütt* 2010: Runoff in Two Semi-Arid Watersheds in a Geoarcheological Context – A Case Study of Naga, Sudan and Resafa, Syria. – Geoarchaeology **25** (6): 815-836

*Bolten, A.* and *O. Bubenzer* 2006: New Elevation Data (SRTM/ASTER) for Geomorphological and Geoarchaeological Research in Arid Regions. – In: *Eitel, B.* (ed.): Holocene Landscape Development and Geoarchaeological Research. – Zeitschrift für Geomorphologie, Supplement Volume **142**. – Stuttgart: 265-279

*Bowler, M.* 1976: Aridity in Australia: Age, Origins and Expression in Aeolian Landforms and Sediments. – Earth-Science Reviews **12**: 279-310

*Bubenzer, O.* and *A. Bolten* 2008: The Use of New Elevation Data (SRTM/ASTER) for the Detection and Morphometric Quantification of Pleistocene Megadunes (Draa) in the Eastern Sahara and the Southern Namib. – Geomorphology **102**: 221-231

*Bubenzer, O., A. Bolten* and *M. Ritter* 2007: Scale-Specific Geomorphometry of Arid Regions: Examples from the Eastern Sahara. – In: *Bollig, M., O. Bubenzer, R. Vogelsang* and *H.-P. Wotzka* (eds.): Aridity, Change and Conflict in Africa. – Proceedings of an International ACACIA Conference held at Königswinter, Germany, October 1-3, 2003. – Colloquium Africanum **2**. – Cologne: 17-34

*Burrough, P.A.* 1986: Principles of Geographical Information Systems for Land Resources Assessment. – Monographs on Soil and Resources Survey **12**. – Oxford

*Burrough, P.A.* and *R.A. McDonnell* 1998: Principles of Geographical Information Systems. – Oxford

*Bussert, R.* 1998: Die Entwicklung intrakratonaler Becken im Nordsudan. – Berliner Geowissenschaftliche Abhandlungen, Reihe A: Geologie und Paläontologie **196**

*Capra, A., S. Gandolfi, L. Laurencich, F. Mancini, A. Minelli, C. Orsini* and *A. Rodríguez* 2002: Multidisciplinary Approach for Archaeological Survey: Explor-

ing GPS Method in Landscape Archaeology Studies. – Journal of Cultural Heritage **3** (2): 93-99

*Cardarelli, E.* and *G. di Filippo* 2009: Integrated Geophysical Methods for the Characterisation of an Archaeological Site (Massenzio Basilica – Roman Forum, Rome, Italy). – Journal of Applied Geophysics **68** (4): 508-521

*Contreras, D.A.* 2008: Reconstructing Landscape at Chavin de Huantar, Peru: A GIS-Based Approach. – Journal of Archaeological Science **36** (4): 1006-1017

*De By, R.A.* 2001: Principles of Geographic Information Systems: An Introductory Textbook. – Enschede

*Drahor, M.G.* 2006: Integrated Geophysical Studies in the Upper Part of Sardis Archaeological Site, Turkey. – Journal of Applied Geophysics **59** (3): 205-223

*Eklundh, L.* and *U. Mårtensson* 1995: Rapid Generation of Digital Elevation Models from Topographic Maps. – International Journal of Geographical Information Systems **9** (3): 329-340

*Estigarribia, J.V.* 2008: The Hafîr as a Water Clarification Device. – Abstract of the Conference Paper, 11th International Conference of Meroitic Studies, Vienna 01.-04.09.2008. – Online available at: http://www.univie.ac.at/afrikanistik/meroe2008/abstracts/Estigarribia.pdf, 08/08/2011

*Folk, R.* and *W. Ward* 1957: Brazos River Bar: A Study in the Significance of Grain Size Parameters. – Journal of Sedimentary Research **27** (1): 3-26

*Forte, M.* 2000: Archaeology and Virtual Micro-Topography: The Creation of DEMs for Reconstructing Fossil Landscapes by Remote Sensing and GIS Applications. – In: *Lock, G.* (ed.): Beyond the Map. Archaeology and Spatial Technologies. – Amsterdam: 199-213

*Fuchs, M.* 2006: Mensch und Umwelt in der Antike Südgriechenlands. – Geographische Rundschau **58** (4): 4-11

*Gabriel, B.* 1997: Zur Quartären Landschaftsentwicklung der Nördlichen Butana (Sudan). – Mitteilungen der Sudanarchäologischen Gesellschaft zu Berlin **7**: 23-30

*Gómez-Ortiz, D., S. Martín-Velázquez, T. Martín-Crespo, A. Márquez, J. Lillo, I. López, F. Carreño, F. Martín-González, R. Herrera* and *M.A. de Pablo* 2007: Joint Application of Ground Penetrating Radar and Electrical Resistivity Imaging to Investigate Volcanic Materials and Structures in Tenerife (Canary Islands, Spain). – Journal of Applied Geophysics **62** (3): 287-300

*Gruen, A.* 2008: Reality-Based Generation of Virtual Environments for Digital Earth. – International Journal of Digital Earth **1** (1): 88-106

*Grunwald, S.* and *P. Barak* 2003: 3D Geographic Reconstruction and Visualization Techniques Applied to Land Resource Management. – Transactions in GIS **7** (2): 231-241

*Günther, T., C. Rücker* and *K. Spitzer* 2006: 3-D Modeling and Inversion of DC Resistivity Data Incorporating Topography – Part II: Inversion. – Geophysical Journal International **166**: 506-517

*Hecht, S.* 2007: Sedimenttomographie für die Archäologie. Geoelektrische und refraktionsseismische Erkundungen für on-site und off-site studies. – In: *Wagner, G.A.* (Hrsg.): Einführung in die Archäometrie. – Berlin et al.: 95-112

*Hengl, T.* and *I.S. Evans* 2009: Mathematical and Digital Models of the Land Surface. – In: *Hengl, T.* and *H.I. Reuter* (eds.): Geomorphometry – Concepts, Software, Applications. – Developments in Soil Science **33**. – Amsterdam et al.: 31-63

*Hinkel, M.* 1991: Hafire im antiken Sudan. – Zeitschrift für Ägyptische Sprache und Altertumskunde **118** (1): 32-48

*Hutchinson, M.F.* 1988: Calculation of Hydrologically Sound Digital Elevation Models. – In: Proceedings of the Third International Symposium on Spatial Data Handling, August 17-19, 1988, Sydney, Australia. – Columbus, Ohio: 117-133

*Hutchinson, M.F.* 1989: A New Procedure for Gridding Elevation and Stream Line Data with Automatic Removal of Spurious Pits. – Journal of Hydrology **106**: 211-232

*Kleinschroth, A.* 1979: Das Reich Kusch und seine wasserwirtschaftlichen Probleme. – Antike Welt **10** (3): 23-30

*Kleinschroth, A.* 1984: Wasserreservoirs im Sudan aus der Zeit der Antike. – Mitteilungshefte des Fachgebiets Hydromechanik der Fakultät für Bauingenieur- und Vermessungswesen der TU München **41**: 75-106

*Kleinschroth, A.* 1986: Die Verwendung des Hafirs im meroitischen Reich. – Beiträge zur Sudanforschung **1**: 79-96

*Kneisel, C.* 2006: Assessment of Subsurface Lithology in Mountain Environments Using 2D Resistivity Imaging. – Geomorphology **80** (1-2): 32-44

*Knödel, K., H. Krummel* und *G. Lange* 1999: Handbuch zur Erkundung des Untergrundes von Deponien und Altlasten. – Berlin

*Kröper, K.* 2006-2007: The End of the Amun-Temple and Beginning of Temple 200 – C14 Dates from Naga. – Cripel, Cahiers de Recherches de l'Institut de Papyrologie et d'Égyptologie de Lille **26**: 231-242

*Leopold, M., T. Plöckl, G. Forstenaicher* and *J. Völkel* 2010: Integrating Pedological and Geophysical Methods to Enhance the Effectiveness of Archaeological Prospection – The Example of a Roman Villa Rustica near Regensburg, Germany. – Journal of Archaeological Science **37** (7): 1731-1741

*Lian, O.B.* and *R.G. Roberts* 2006: Dating the Quaternary: Progress in Luminescence Dating of Sediments. – Quaternary Science Reviews **25** (19-20): 2449-2468

*Mitas, L.* and *H. Mitášová* 1999: Spatial Interpolation. – In: *Longley, P., M.F. Goodchild, D.J. Maguire* and *D.W. Rhind* (eds.): Geographical Information Systems: Principles, Techniques, Management and Applications. – Chichester: 481-492

*Mitášová, H.* and *J. Hofierka* 1993: Interpolation by Regularized Spline with Tension. II: Application to Terrain Modeling and Surface Geometry Analysis. – Mathematical Geology **25** (6): 657-669

*Murray, A.S.* and *A.G. Wintle* 2000: Luminescence Dating of Quartz Using an Improved Single-Aliquot Regenerative-Dose Protocol. – Radiation Measurements **32** (1): 57-73

*Neal, A.* 2004: Ground-Penetrating Radar and its Use in Sedimentology: Principles, Problems and Progress. – Earth-Science Reviews **66**: 261-330

*Nichols, G.* 1999: Sedimentology and Stratigraphy. – Oxford

*Nikolakopoulos, K., E. Kamaratakis* and *N. Chrysoulakis* 2006: SRTM vs. ASTER Elevation Products. Comparison for two Regions in Crete, Greece. – International Journal of Remote Sensing **27** (21): 4819-4838

*Peckham, R.J.* and *G. Jordan* (eds.) 2007: Digital Terrain Modelling. Development and Applications in a Policy Support Environment. – Berlin et al.

*Peeters, I., T. Rommens, G. Verstraeten, G. Govers, A. van Rompaey, J. Poesen* and *K. van Oost* 2006: Reconstructing Ancient Topography through Erosion Modelling. – Geomorphology **78**: 250-264

*Rapp, G.* and *C.L. Hill* 2006: Geoarchaeology. The Earth-Science Approach to Archaeological Interpretation. – 2nd edition. – London

*Reimann, T., M. Naumann, S. Tsukamoto* and *M. Frechen* 2010: Luminescence Dating of Coastal Sediments from the Baltic Sea Coastal Barrier-Spit Darss-Zingst, NE Germany. – Geomorphology **122** (3-4): 264-273

*Reynolds, J.M.* 1997: An Introduction to Applied and Environmental Geophysics. – Chichester

*Rücker, C., T. Günther* and *K. Spitzer* 2006: 3-D Modelling and Inversion of DC Resistivity Data Incorporating Topography. Part I: Modelling. – Geophysical Journal International **166** (2): 495-505

*Sandmeier, R.* 1997: Reflex Help Notes, Sandmeier Software. – http://www.sandmeier-geo.de, 22/03/2010

*Scheibner, T.* 2004: Neue Erkenntnisse zur Wasserversorgung von Musawwarat es Sufra (I). Das übergeordnete Wasserversorgungssystem: Teil I: Wassergewinnung und -speicherung. – Mitteilungen der Sudanarchäologischen Gesellschaft zu Berlin e.V. **15**: 39-65

*Schön, J.* 1983: Petrophysik. Physikalische Eigenschaften von Gesteinen und Mineralen. – Stuttgart

*Schöwer, R.* 2007: Das Baustellenhandbuch für Aufmaß und Mengenermittlung. – Merching

*Schütt, B.* and *J. Krause* 2009: Comparison of Proxy-Based Palaeoenvironmental Reconstructions and Hindcast-Modelled Annual Precipitation – a Review of Holocene Palaeoenvironmental Research in the Central Sahara. – In: *Baumhauer, R.* and *J. Runge* (eds.): Holocene Palaeoenvironmental History of the Central Sahara. – Palaeoecology of Africa **29**. – Boca Raton: 23-37

*Schütt, B., J. Berking, F. Frechen, P. Frenzel, A. Schwalb* and *C. Wrozyna* (2010): Late Quaternary Transition from Lacustrine to a Fluvio-Lacustrine Environment in the North-Western Nam Co, Tibetan Plateau, China. – Quaternary International **218** (1-2): 104-117

*Shaaban, F.F.* and *F.A. Shaaban* 2001: Use of Two-Dimensional Electric Resistivity and Ground Penetrating Radar for Archaeological Prospecting at the Ancient Capital of Egypt. – Journal of African Earth Sciences **33** (3-4): 661-671

*Siart, C., B. Eitel* and *D. Panagiotopoulos* 2008: Investigation of Past Archaeological Landscapes using

Remote Sensing and GIS: A Multi-Method Case Study from Mount Ida, Crete. – Journal of Archaeological Science **35**: 2918-2926

*Siart, C., O. Bubenzer* and *B. Eitel* 2009: Combining Digital Elevation Data (SRTM/ASTER), High Resolution Satellite Imagery (Quickbird) and GIS for Geomorphological Mapping: A Multi-Component Case Study on Mediterranean Karst in Central Crete. – Geomorphology **112**: 106-121

*Siart, C., S. Hecht, I. Holzhauer, R. Altherr, H.P. Meyer, G. Schukraft, B. Eitel, O. Bubenzer* and *D. Panagiotopoulos* 2010: Karst Depressions as Geoarchaeological Archives: The Palaeoenvironmental Reconstruction of Zominthos (Central Crete), Based on Geophysical Prospection, Sedimentological Investigations and GIS. – Quaternary International **216** (1-2): 75-92

*Stuiver, M., P. Reimer* and *T. Braziunas* 1998: High-Precision Radiocarbon Age Calibration for Terrestrial and Marine Samples. – Radiocarbon **40** (3): 1127–1151

*Telford, W.M., L.P. Geldart* and *R.E. Sheriff* 1990: Applied Geophysics. – Cambridge

Thales Navigation 2004: ProMark 2 System. User Guide. – Online available at: http://e-topo.web.auth. gr/TOMEIS_INDEX/TOMEASA/Pikridas/give/ashtech_manual/promarkmanual.pdf, 20/12/2011

*Tonini, A., E. Guastaldi, G. Massa* and *P. Conti* 2008: 3-D Geo-Mapping based on Surface Data for Preliminary Study of Underground Works: A Case Study in Val Topina (Central Italy). – Engineering Geology **99** (1-2): 61-69

*Ullrich, B., C. Meyer* und *A. Weller* 2007: Geoelektrik und Georadar in der archäologischen Forschung: Geophysikalische 3D-Untersuchungen in Munigua (Spanien). – In: *Wagner, G.A.* (Hrsg.): Einführung in die Archäometrie. – Berlin et al.: 75-93

*Vogel, S.* and *M. Märker* 2009: Reconstructing the Roman Topography and Environmental Features of the Sarno River Plan (Italy) before the AD 79 Eruption of Somma-Vesuvius. – Geomorphology **115** (1-2): 67-77

*Wainwright, J.* and *M. Mulligan* 2004: Environmental Modelling. Finding Simplicity in Complexity. – Oxford

*Weinstein-Evron, M., A. Beck* and *M. Ezersky* 2003: Geophysical Investigations in the Service of Mount Carmel (Israel) Prehistoric Research. – Journal of Archaeological Science **30** (10): 1331-1341

*Wenske, D., M. Böse, M. Frechen* and *C. Lüthgens* 2009: Late Holocene Mobilisation of Loess-Like Sediments in Hohuan Shan, High Mountains of Taiwan. – Quaternary International **234** (1-2): 174-181

*Wildung, D.* and *K. Kröper* 2006: Naga – Royal City of Ancient Sudan. – Berlin

*Wolf, S., P. Wolf, H.U. Onasch, C. Hof* und *U. Nowotnick* 2008: Meroë und Hamadab – Zwei Städte im Mittleren Niltal in den Jahrhunderten um die Zeitenwende: Bericht über die Arbeiten zwischen 1999 und 2007 = Meroe and Hamadab – Two Cities in the Middle Nile Valley in the Centuries around the Beginning of Common Era. Report on Activities between 1999 and 2007. – Archäologischer Anzeiger **2**: 157-230

*Zhou, Q., B. Lees* and *G. Tang* (eds.) 2008: Advances in Digital Terrain Analysis. – Berlin et al.

*Summary: Geoarchaeological Methods for Landscape Reconstruction at the Excavation Site of Naga, Central Sudan*

In central and northern Sudan several great kingdoms had existed since the late Bronze Age. Naga was one of the major cities during the phase of the Meroitic culture, some 2000 years ago. Located in the dry savanna, about 40 km south of the Nile, Naga is unique, mainly because of its "Great Hafir", a hand-dug reservoir, with a capacity of 37,000 $m^3$ for collecting surface runoff. The present study employs techniques from geophysics, terrain modelling and environmental analytics to evaluate field data for a comprehensive landscape reconstruction. Samples from a 170 cm deep trench in the hafir reveal an OSL age of 700 ± 180 years at 40 cm depth and a radiocarbon age of 695 ± 25 years BP at 80 cm depth, which are consistent with our idea of the Post-Meroitic siltation of the basin.

*Zusammenfassung: Geoarchäologische Methoden zur Landschaftsrekonstruktion an der Ausgrabungsstätte von Naga, Zentralsudan*

Der zentrale und nördliche Sudan war seit der späten Bronzezeit durch mehrere große Königreiche geprägt. Die Stadt Naga zählte dabei, rund um die Zeitenwende um Christi Geburt, während der Meroitischen Zeit, zu

den größeren und wichtigen Städten. Gelegen in der Trockensavanne und ca. 40 km südlich des Nils, ist die Anlage der Stadt und ihrer Infrastruktur nahezu einzigartig. Dies bezieht sich im Besonderen auf das große, handgegrabene Wasserauffangbecken, das sogenannte „Große Hafir von Naga", mit einem Speichervolumen von 37.000 m³. Die vorliegende Studie bedient sich im Wesentlichen Methoden der Geophysik, der Landschaftsmodellierung und der Umweltanalytik; ihre Datengrundlage wurde bei mehreren Feldkampagnen erhoben. Aus Datierungs-Proben eines 170 cm tiefen Profils im Hafirbecken ergeben sich ein OSL-Alter von 700 ± 180 J.v.h. in 40 cm Tiefe und ein Radiokarbonalter von 695 ± 25 J.v.h. in 80 cm Tiefe; diese Ergebnisse bestätigen unsere Annahme, dass das Hafir in post-meroitischer Zeit aufsedimentiert wurde.

*Résumé: Méthodes géoarchéologiques pour la reconstruction du paysage au site archéologique de Naga, au centre du Soudan*

Pendant l'âge de bronze, des grands royaumes ont existés au nord et au centre du Soudan. Naga fut l'une des plus grandes villes importantes de l'époque marquée par la culture méroïtique, prospérant vers l'époque de la naissance de Jésu Christ. Aujourd'hui, situées à 40 kilomètres au sud du Nil, en zone de savane sèche, les ruines de la ville de Naga sont des témoins uniques en terme d'ingéniosité de toutes ses constructions. Un excellent exemple en est le grand bassin d'irrigation de Naga, entièrement creusé à la main dont la capacité est de 37,000 m³. L'étude présentée ici se base sur des différentes méthodes géophysiques, une modélisation numérique du terrain ainsi que sur des analyses environnementales. Les échantillons de ces analyses ont été relevés au cours de plusieurs études de terrain. Les âges des sédiments prélevés à 40 cm de profondeur (700 ± 180 a) et 80 cm (695 ± 25 a BP) dans un fossé de 170 cm de profondeur ont été déterminés grâce à la méthode OSL. Ces résultats correspondent à l'idée que le bassin fut couvert avec des sédiments au temps post-méroïtique.

*Dr. Jonas Berking, Julia Meister M.Sc., Michael Schott, Prof. Dr. Brigitta Schütt*, Freie Universität Berlin, Department of Earth Sciences, Physical Geography, Malteserstraße 74-100, 12249 Berlin, Germany, Jonas.Berking@fu-berlin.de, Julia.Meister@fu-berlin.de, brigitta.schuett@fu-berlin.de

*Burkart Ullrich, Prof. Dr. Georg Kaufmann*, Freie Universität Berlin, Department of Earth Sciences, Institute of Geological Sciences, Geophysics Section, Malteserstr. 74-100, 12249 Berlin, Germany, ullrich@geophysik.fu-berlin.de, kaufmann@geophysik. fu-berlin.de

Manuscript submitted: 03/08/2010
Accepted for publication: 29/01/2011